

SeaMo: A Multi-Seasonal and Multimodal Remote Sensing Foundation Model

Xuyang Li^{a,b}, Danfeng Hong^{a,b,*}, Chenyu Li^c, Jocelyn Chanussot^d

^a*Aerospace Information Research Institute, Chinese Academy of Sciences, Beijing 100094, China*

^b*School of Electronic, Electrical and Communication Engineering, University of Chinese Academy of Sciences, Beijing 100049, China*

^c*School of Mathematics, Southeast University, Nanjing 211189, China*

^d*INRIA, Montbonnot Saint Martin 38330, France*

Abstract

Remote Sensing (RS) data contains a wealth of multi-dimensional information crucial for Earth observation. Owing to its vast volume, diverse sources, and temporal properties, RS data is highly suitable for the development of large Visual Foundation Models (VFMs). VFMs act as robust feature extractors, learning from extensive RS data, and are subsequently fine-tuned for deployment in various geoscientific tasks. However, current VFMs in the RS domain are predominantly pretrained and tailored exclusively for specific characteristics of RS imagery, neglecting the potential of utilizing the multi-dimensional properties of RS data. Therefore, in this work, we propose SeaMo, a pioneering visual foundation model that integrates multi-seasonal and multimodal information in the RS field. SeaMo is designed to harness multiple properties of RS data. Within the masked image modeling framework, we employ non-aligned cropping techniques to extract spatial properties, use multi-source inputs for multimodal integration, and incorporate temporal-multimodal fusion blocks for effective assimilation of multi-seasonal data. SeaMo explicitly models the multi-dimensional properties of RS data, making the model more comprehensive, robust, and versatile. We applied SeaMo to several downstream geoscience tasks, which demonstrated exceptional performance. Extensive ablation studies were conducted to validate the model's superiority.

Keywords: Remote sensing, foundation models, multimodal, deep learning, self-supervised learning

1. Introduction

Remote sensing is a technology that enables the measurement of soil or crop characteristics using platforms such as UAVs, airplanes, or satellites [1]. The data acquired through remote sensing technology are utilized to study social phenomena, land use dynamics, and changes in landscapes for scientific analysis and modeling purposes. Currently, hundreds of remote sensing satellites continuously monitor the Earth's surface, generating large-scale time series datasets. These datasets, characterized by their heterogeneity and incorporation of multiple sources, in-

cluding spectral data, radar data, and meteorological data, provide a rich repository of physical geographic information, embodying the typical traits of big data [2]. The research on image data in remote sensing currently faces several challenges and focal points:

(1) Integration of data from diverse sources for varied geoscientific applications: Different methods of capturing how electromagnetic radiation interacts with Earth surface materials provide unique datasets [3]. Optical data, by measuring radiation across many wavelengths, offers detailed spectral information that characterizes the material composition of objects. Synthetic Aperture Radar (SAR) data, by transmitting and receiv-

*Corresponding author

Email address: hongdf@aircas.ac.cn (Danfeng Hong)

ing longer wavelength electromagnetic pulses, can assess the geometry, roughness, and electrical properties of objects. Given the significant heterogeneity between these data sources, simple transformations and combinations of data dimensions are insufficient to fully exploit this information [4]. Thus, a key area of focus is how to extract valuable geoscientific information from these diverse datasets that can meet human needs.

(2) Effective modeling and utilization of spatio-temporal data: The spatio-temporal structure of satellite imagery involves the availability of multiple temporally-spaced images for the same location. This rich spatio-temporal characteristic of remote sensing data enables the analysis of changes in physical geography, and land use, and offers insights into geological structures or socio-economic conditions [5]. However, the low information density of spatio-temporal data, due to low spatial resolution and long intervals between observations, makes it challenging to capture temporal dynamics with simple techniques. Therefore, how to effectively mine geoscientific information from spatio-temporal data with low information density remains a research hotspot.

Visual Foundation Models (VFMs) refer to large-scale neural networks that are pretrained on vast datasets, typically using self-supervised learning methods. VFMs act as robust and powerful feature extractors and can be fine-tuned with minimal effort for various downstream tasks [6]. Given the inherent big data characteristics and the complex information contained within remote sensing data, the vast data landscape of remote sensing offers significant opportunities for the implementation of VFMs in earth observation. Currently, several VFMs have been introduced in the field of remote sensing, demonstrating performance that surpasses traditional deep learning models across a broad range of geoscientific tasks. This advancement has led to significant breakthroughs in the mining and extraction of remote sensing information. However, these models still face several challenges and deficiencies:

(1) Lack of geoscientific attributes: Some VFMs in the remote sensing domain are derived from computer vision technologies and often involve simplistic transformations of remote sensing data to adapt it to algorithmic requirements. This approach generally leads to insufficient exploration of the geoscientific properties inherent in remote sensing data, resulting in a gap in feature extraction capabilities. For instance, DINO-MC [7] employs basic data augmentation and uses Contrastive Learning (CL) for pretraining. Similarly, RSVA [8] straightforwardly adapts the Masked Autoencoders from the computer vision domain for pretraining in remote sensing.

(2) Single-dimension data modeling: While most VFMs acknowledge the unique characteristics of remote sensing data, they typically focus on a single dimension, such as spatial or temporal attributes [9]. For instance, SeCo [10] and CaCo [11] exploit the temporal dynamics of RS images, employing Contrastive Learning (CL) to capture time-invariant features at specific geo-locations. RingMo [12] introduces Masked Image Modeling (MIM) to the RS domain, targeting small objects with a sparse masking strategy. SatMAE [13] employs a group combination masking strategy within the Masked Autoencoders (MAE) framework [14], enriching its handling of multi-spectral or temporal data. Similarly, SpectralGPT [15] innovatively addresses the spectral sequence attributes of images, employing a 3D mask strategy focused on spectral sequence reconstruction. ScaleMAE [16] and SatMAE++ [17] adjust to the varying sizes and resolutions of RS images, designing multiple image-size reconstruction targets. CROMA [18] pretrains aligned radar and optical images using both CL and MIM methods. The objective is to leverage the multimodal attributes of remote sensing to enhance the model’s feature extraction capabilities.

(3) Non-explicit modeling multi-dimensional data attributes: Some VFMs consider multi-dimensional attributes, yet their approach to modeling and pretraining is more akin to stacking and assembling

rather than explicitly modeling from a remote sensing and geoscientific perspective [19, 20]. This often leads to a superficial integration of multidimensional data, which does not fully exploit the synergistic potential of combining spatial, temporal, and spectral characteristics inherent in remote sensing data. For instance, Skysense [19] integrates information from various remote sensing (RS) data modalities, temporal information, and geographic location within the framework of contrastive learning. It employs contrastive learning for multimodal spatial feature extraction and utilizes positional encodings to embed temporal and geographic information, surpassing previous models. However, the integration of its multidimensional attributes is not fully realized. Specifically, the model optimizes the data learning from multiple separate aspects rather than in a holistic manner. The embedding of positional encodings serves merely as an insertion of prior knowledge rather than facilitating active knowledge learning and discovery.

From the analysis of existing research questions and deficiencies in remote sensing visual foundation models, we believe it is necessary to establish a visual foundation model that not only effectively utilizes multi-source satellite data but also explicitly models the spatial and temporal properties of the data. Furthermore, this model should be optimized using a unified objective during training. Therefore, we introduce **SeaMo**, a pioneering foundation model in the RS field that effectively integrates spatial, multimodal, and multi-seasonal information. To enhance the spatial information density, we utilize unaligned crop techniques as data augmentation methods. To leverage the complementary strengths of multimodal satellite data during model pretraining, we employ a unified encoder that allows for multisource data, which is then jointly input into the model. The integration of information is facilitated through self-attention mechanisms. To enhance time-invariant representations, we have designed a temporal fusion block with cross-attention mechanisms

that effectively integrates multiple spatial-temporal data streams. Finally, the model is optimized using a unified masked modeling approach. Our contributions are outlined as follows:

- We propose a unified Masked Image Modeling (MIM) framework that learns representations from multimodal and multi-seasonal data. For multimodal data, we utilize a concat-style strategy, while for multi-seasonal data, we implement a siamese network approach.
- We have developed a Temporal-Multimodal (TM) fusion block, a cascade-style component that effectively integrates different seasonal and multimodal information during pretraining.
- Our pretraining methodology adopts a multi-stage strategy that incrementally progresses from learning unimodal representations to multimodal and then to seasonal-multimodal representations. This step-by-step approach ensures a comprehensive understanding of the multidimensional features of RS data.
- The proposed foundation model has been successfully transferred to various downstream geoscientific applications across different modalities, demonstrating its robust performance. Additionally, detailed ablation studies have been conducted to further substantiate the superior capabilities of the model.

2. Related Work

2.1. Self-supervised visual representation learning

Self-supervised learning is a technique for learning generalizable visual representations through various pretext tasks without the need for annotations during pretraining [21]. Initially, this approach utilized straightforward tasks such as image colorization, image rotation prediction, or solving jigsaw puzzles [22, 23, 24]. In recent years, Contrastive Learning (CL) and Masked Image Modeling

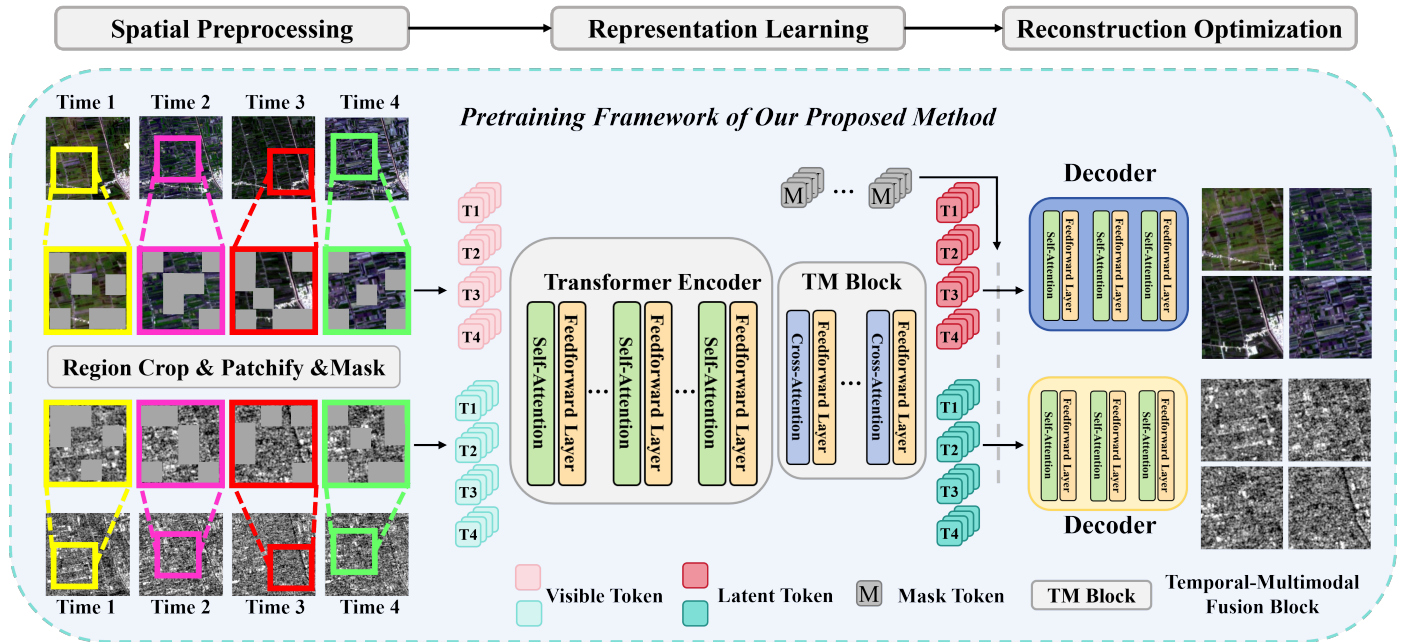


Figure 1: **Pretraining Workflow of the SeaMo Foundation Model.** The SeaMo architecture integrates three primary components: encoders, temporal-multimodal fusion blocks (TM blocks), and decoders. Our approach incorporates a partially overlapping cropping strategy, ensuring that images from the same temporal instance are cropped identically across various modalities, while images from different instances exhibit partial overlaps. These processed images then serve as inputs to the network. Following the Masked Autoencoder paradigm, only visible tokens are processed by the encoder. The TM block effectively merges features from multiple seasons and modalities, culminating in modality-specific decoders that reconstruct the initially masked regions of the images.

(MIM) have become predominant self-supervised techniques for pretraining large foundation models. CL is designed to capture feature invariance across a batch of images by differentiating between identical and modified images using data augmentation techniques, with implementations like SimCLR [25] and MoCo [26]. Conversely, MIM focuses on revealing spatial correlations by reconstructing masked patches within a single image, as seen in methods like SimMIM [27] and MAE [14]. These techniques are complementary. Methods such as SiameseIM [28] and MimCo [29] successfully integrate both CL and MIM to capture data features, leading to superior performance in both linear probing and fine-tuning evaluations.

2.2. Masked autoencoders

Masked autoencoders (MAE) [14] are a variant of denoising autoencoders that learn representations by reconstructing the original image from its masked inputs. This method is inspired by the self-masking pretraining mech-

anism found in the BERT[30] language model. It introduces random masks into the image inputs, requiring the network to reconstruct the original image from a partially masked version as a means of pretraining on image data. Typically, the model employs an encoder-decoder structure, and after pretraining, only the encoder is used as the backbone for downstream tasks. In masked image modeling, the encoder-decoder structure is usually asymmetric: the encoder is designed to learn high-level representations, while the decoder focuses on learning how to reconstruct the target. MAEs have proven effective across various vision benchmarks, prompting their adaptation in numerous studies across several data modalities. These include multimodal images [31], video data [32], medical data [33], remote sensing data [9] and meteorological data.[34].

3. Proposed Method

We aim to develop a foundation model, SeaMo, designed to learn robust temporal and spatial representations

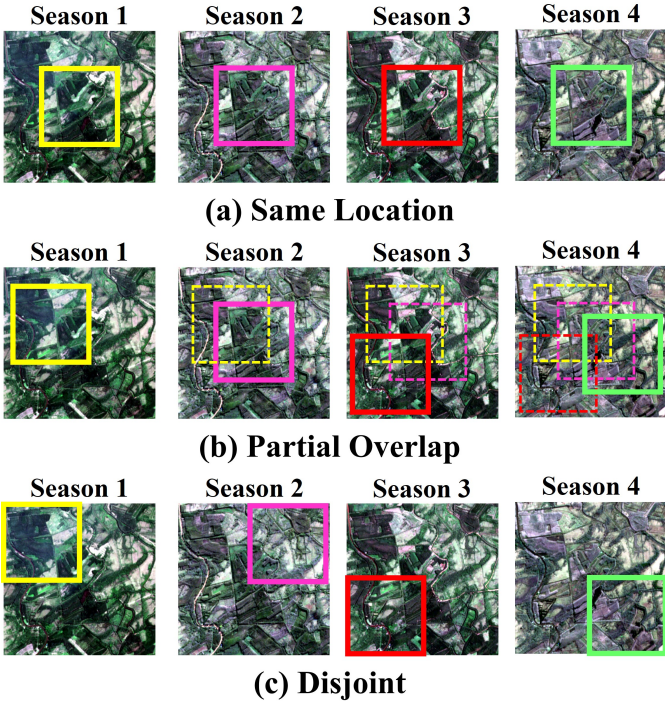


Figure 2: **Different crop strategies for seasonal data.** The solid boxes indicate the images cropped and input into the network. (a) Images from different seasons are cropped to the same section. (b) Images from different seasons are cropped according to a specific proportion of the full image but ensure that some areas overlap. (c) Images from different seasons are cropped without any overlap.

from multi-seasonal and multimodal remote sensing data. SeaMo consists of three principal components: encoders, temporal-multimodal fusion blocks, and decoders, as illustrated in Figure 1. Our research utilizes the SSL4EO-S12 dataset [35], which includes 12-channel multispectral optical imagery from Sentinel-2 and 2-channel SAR backscatter data from Sentinel-1.

3.1. Method overview of SeaMo

3.1.1. Tokenizer

We denote optical inputs and SAR inputs as $\mathbf{I}_O, \mathbf{I}_R \in \mathbb{R}^{T \times C \times H \times W}$, where T represents the number of images in a temporal sequence. The temporal image pairs are fed into the model season by season, denoted separately as $\mathbf{I}_O^t, \mathbf{I}_R^t \in \mathbb{R}^{C \times H \times W}$, $t = 1, 2, \dots, T$. Each type of data undergoes a modality-specific tokenizer into L encodings $\mathbf{E}_O^t, \mathbf{E}_R^t \in \mathbb{R}^{L \times D}$, $t = 1, 2, \dots, T$ with fixed sinusoidal positional embeddings [36].

3.1.2. Mask operation

Next, a masking operation is conducted on the patches to distinguish between unmasked and masked patches. This is represented as $[\mathbf{O}_{visible}^t, \mathbf{O}_{masked}^t] = \mathbb{M} \odot \mathbf{E}_O^t$ and $[\mathbf{R}_{visible}^t, \mathbf{R}_{masked}^t] = \mathbb{M} \odot \mathbf{E}_R^t$, where $\mathbb{M} \in \{0, 1\}^{L \times D}$ is a binary mask that indicates the patches to be masked. Notably, we employ a consistent masking strategy for images from different sensors captured at the same time and a random masking strategy for images from the same sensor but captured at different times. This approach enhances the reconstruction challenge, encouraging the model to learn more robust representations.

3.1.3. Encoder

We concatenate the visible tokens from two modalities and input them into the encoder Φ , denoted as $\{\mathbf{F}_O^t, \mathbf{F}_R^t\} = \Phi(\text{concat}[\mathbf{O}_{visible}^t, \mathbf{R}_{visible}^t])$. This encoder utilizes plain vision transformer blocks [37]. Following the random masking process, $\mathbf{O}_{visible}^t$ and $\mathbf{R}_{visible}^t$ represent tokens that vary not only in their modality but also in spatial attributes. Consequently, the encoder’s self-attention mechanism is capable of extracting features and building the relationships of all visible tokens between multimodal and spatial dimensions.

3.1.4. Temporal-Multimodal fusion block

The output from the encoder generates multimodal features at distinct time points, represented as $\{\mathbf{F}_O^t, \mathbf{F}_R^t\}$, $t = 1, 2, \dots, T$. Although seasonal images are processed through the encoder, the neural network cannot currently explicitly learn time-invariant representations, leaving temporal features underutilized. To address this, we introduce the Temporal-Multimodal (TM) fusion block (see Figure 3), inspired by SiamMAE [38], which is designed to explicitly learn temporal correspondences in videos. In this block, each modality data participates not only in the interaction of data fusion at the current time point but also contributes to the fusion at the subsequent time point. Algorithm 1 provides the pseudocode for the

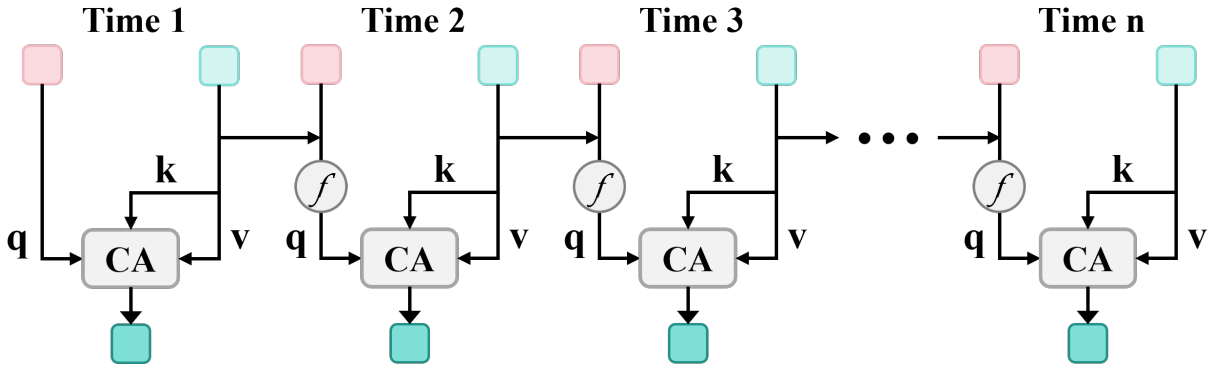


Figure 3: **An illustration of the Temporal-Multimodal (TM) block.** In this block, data from each modality not only engages in data fusion interactions at the current season but also influences the fusion process in subsequent seasons.

Temporal-Multimodal (TM) fusion block. Since all images are to be reconstructed, the visible tokens of each image act as the query. Tokens from other modalities of the same season, combined with tokens from the previous season, serve as the key and value. Cross-attention is then employed to facilitate interactions across temporal and modal dimensions.

3.1.5. Decoder

The output from the TM block consists of features from distinct modalities at each time step, denoted as $\{\mathbf{H}_O^t, \mathbf{H}_R^t\}, t = 1, 2, \dots, T$. We design modality-specific decoders for each modality’s features. For unimodal features at different time steps, the decoders are weight-sharing; specifically, all optical features \mathbf{H}_O^t , with added mask tokens and positional embeddings, serve as separate inputs to the optical decoders to reconstruct the original images \mathbf{I}_O^t . SAR modality data are also employed in the same procedure. We compute the mean squared error (MSE) between the reconstructed and original images only for the masked patches of all images [14]. Then, we sum these losses together to form the final loss.

3.2. Crop Strategies for Spatial Attribute Mining

Despite the rich geospatial information contained in remote sensing images, the low spatial resolution and the long distances involved result in a low information density

of spatial data. Consequently, relying solely on image-level self-supervised learning makes it challenging to learn representations of spatial details. Temporal data capture geographical information of the same location at different times. When inputting them into the network, we can apply different cropping strategies to multi-temporal data. One approach is to use the same crop area for all temporal images (as shown in Figure 2(a)). Alternatively, the multi-temporal images can be partially overlapping spatially (as shown in Figure 2(b)), or the four temporal images can be entirely non-overlapping (as shown in Figure 2(c)).

From the perspective of remote sensing, we posit that, except for changes due to human activities, the geological attributes of the same area in the ecological environment remain constant over time. Therefore, by performing partially overlapping cropping on same-modality images at different times, which means the multi-temporal images input into the network do not completely overlap spatially, we can constrain the network to explore correlations that exist between data in non-overlapping regions. From a computer vision standpoint, CropMAE [39] has demonstrated that using locally correlated cropping in Masked Autoencoder (MAE) tasks can enhance a model’s ability to learn spatial representations.

In Section 4.5.1, we evaluated three cropping methods illustrated in Figure 2. The results indicate that partially overlapping data inputs lead to the best model perfor-

Algorithm 1 Temporal-Multimodal Fusion Block

```
1: Input: Encoded features  $\mathbf{F}_O^t, \mathbf{F}_R^t$  for  $t = 1, 2, \dots, T$ 
2: Output: Temporally and modally fused features  $\mathbf{H}_O^t, \mathbf{H}_R^t$  for  $t = 1, 2, \dots, T$ 
3: for  $t = 1$  to  $T$  do
4:   Multimodal Fusion at Time  $t$ 
5:    $\mathbf{H}_O^t \leftarrow CA(\text{query} = \mathbf{F}_R^t, [\text{key}, \text{value}] = \mathbf{F}_O^t)$ 
6:    $\mathbf{H}_R^t \leftarrow CA(\text{query} = \mathbf{F}_O^t, [\text{key}, \text{value}] = \mathbf{F}_R^t)$ 
7:   if  $t < T$  then
8:     Temporal Fusion for Next Time Point
9:      $\mathbf{H}_O^{t+1} \leftarrow CA(\text{query} = f[\mathbf{F}_R^{t+1}, \mathbf{F}_O^t], [\text{key}, \text{value}] = \mathbf{F}_O^{t+1})$ 
10:     $\mathbf{H}_R^{t+1} \leftarrow CA(\text{query} = f([\mathbf{F}_O^{t+1}, \mathbf{F}_R^t], [\text{key}, \text{value}] = \mathbf{F}_R^{t+1})$ 
11:   end if
12: end for
13: Note:  $CA$  denotes the cross-attention layer and  $f$  represents linear layers used to fuse features.
```

mance. We believe that using the same region for all temporal images makes the reconstruction task overly simple while employing four entirely non-overlapping images makes it difficult for the model to discover correlations within the data.

3.3. Progressive pretraining strategy

As depicted in Figure 4 (left), relying solely on a single Masked Image Modeling (MIM) model, the unimodal pretraining procedure lacks interaction across modalities. This approach leads to the model learning multimodal representation implicitly and sub-optimally. Drawing inspiration from models such as GFM [40], SpectralGPT [15], and other MAE-based works [41, 42], we introduce a progressive pretraining strategy for SeaMo. The pretraining process comprises two phases: initially focusing on learning single-time features and subsequently advancing to multi-time features.

3.3.1. Single-time point multimodal learning

In the initial phase, depicted in Figure 4 (middle), we use data from only a single time point. The first seasonal dataset, which comprises 25% of the total data, is employed for pretraining without temporal information. During this stage, visible tokens from two modalities are concatenated and input into the encoder. As spatial in-

formation is crucial for remote sensing interpretation, the focus here is to enable the model to capture both spatial and multimodal features at this singular time point. The foundational understanding of spatial characteristics provides a valuable basis for subsequent phases aimed at developing time-invariant representations.

3.3.2. Multi-time flow multimodal learning

In this stage, we initialize the model using pretrained weights from the single-time learning stage. The inputs for this phase include multi-seasonal and multimodal images. Following initial processing by the encoder, Temporal-Multimodal (TM) blocks are integrated to facilitate interactions among seasonal data, as depicted in Figure 4 (right). Within these blocks, multi-seasonal and multimodal tokens are explicitly fused and interact through cross-attention layers in a time flow sequence. TM blocks are essential for enabling the model to acquire time-invariant multimodal representations, significantly enhancing model performance. This functionality has been validated through our ablation studies in Section 4.5. After pretraining, the encoder serves as the backbone for downstream tasks, while the TM blocks and decoders are discarded.

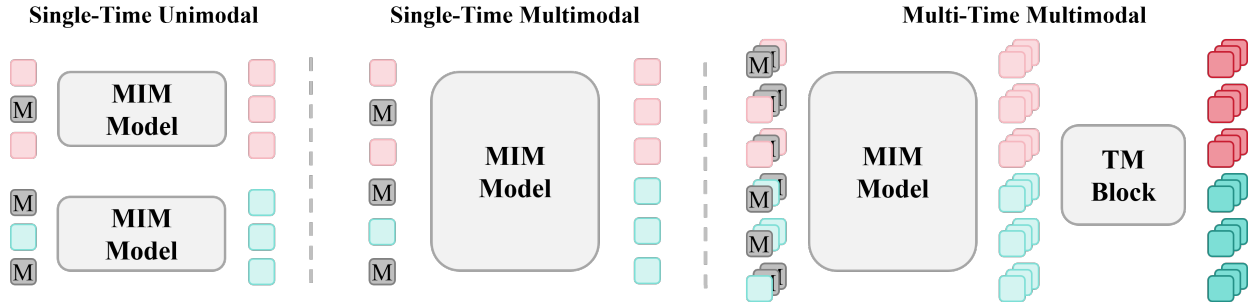


Figure 4: **Three distinct multimodal pretraining strategies.** **Left:** The MIM model is weight-sharing, however, lacks interaction across different modalities. **Middle:** Data from two modalities are concatenated and then fed into the MIM model. **Right:** A time series of multimodal images are concatenated (modal-concat) and then processed by the MIM model, followed by a Temporal-Multimodal (TM) block to strengthen representation learning.

Table 1: **Fine-tuning (FT) results on three optical classification benchmarks: EuroSAT, fMoW-S2 and BigEarthNet.** On the fMoW-S2 and BEN datasets, we default to using only 10% of the training data to fine-tune the models. * denotes the results obtained by fine-tuning with all training data, rather than only 10% of the data.

Dataset	Metrics	GASSL	SeCo	MAE	DINO	I-JEPA	SatMAE	SpectralGPT	Satlas	CROMA	DOFA	ours
		ResNet50	ResNet50	ViT-S	ViT-S	ViT-B	ViT-B	ViT-B	Swin-B	ViT-B	ViT-B	ViT-B
EuroSAT	Acc.	96.96	97.23	98.78	99.01	99.20	99.20	99.21	98.97	99.22	99.30	99.37
fMoW-S2	Acc.	50.69*	51.65*	51.79	52.79	53.54	57.20	55.28	57.95	54.47	58.10	58.25
BEN	mAP	79.24	82.62	86.15	87.04	85.92	85.94	87.50	82.80	87.58	86.75	88.54

4. Experiments

In this section, we first describe the dataset utilized for pretraining and outline the pretraining setup for our model, SeaMo. Then we report and compare the performance of SeaMo and other models across a range of downstream tasks, including single/multi-label classification, semantic segmentation, and change detection involving various modalities. The results demonstrate SeaMo’s exceptional performance and generalization capabilities. Additionally, we present ablation studies that explore different model configurations, hyperparameter settings, and choices of pretraining strategies.

4.1. Pretraining experimental setup

4.1.1. Pretraining data

We pretrained our model SeaMo on the SSL4EO-S12 [35] dataset, a comprehensive multimodal, multi-temporal dataset designed for self-supervised learning in Earth Observation. This dataset targets diverse urban and suburban landscapes and excludes images with high cloud

cover. It includes 3 million images from Sentinel-2 (multi-spectral, levels 1C and 2A) and Sentinel-1 (SAR), covering 250,000 locations worldwide. Each location is documented with four seasonal snapshots, capturing the variability within a calendar year. The images are uniformly sized at 264×264 pixels. For pretraining, we utilize products from Sentinel-2 level-2A, which provides 12 multi-spectral channels, and Sentinel-1 SAR, which includes two channels (VV and VH).

4.1.2. Pretraining implementation

We utilize the ViT-Base model as the backbone for our pretraining process. As detailed in Section 3.3, our approach incorporates a progressive pretraining strategy, which enhances data utilization and facilitates the learning of representations. Initially, for the single-time point multimodal learning stage, we use only the first season’s data, which represents 25% of the total dataset, and train without the Temporal-Multimodal (TM) block for 20 epochs. In the subsequent multi-time flow multimodal learning stage, we incorporate the TM block and

Table 2: **Linear-probing (LP) results on three optical classification benchmarks: EuroSAT, fMoW-S2 and BigEarthNet (BEN).** On the fMoW-S2 and BEN datasets, we default to using only 10% of the training data to fine-tune the models.

Dataset	Metrics	GASSL	SeCo	MAE	DINO	I-JEPA	SatMAE	SpectralGPT	Satlas	CROMA	DOFA	ours
		ResNet50	ResNet50	ViT-S	ViT-S	ViT-B	ViT-B	ViT-B	Swin-B	ViT-B	ViT-B	ViT-B
EuroSAT	Acc.	86.52	87.62	86.08	87.04	85.92	86.87	87.92	91.14	91.75	92.20	93.46
fMoW-S2	Acc.	33.82	34.41	27.69	32.64	32.35	35.17	35.80	37.81	38.17	37.51	37.95
BEN	mAP	76.41	77.97	75.94	81.58	80.80	79.36	81.05	82.11	83.41	82.45	82.73

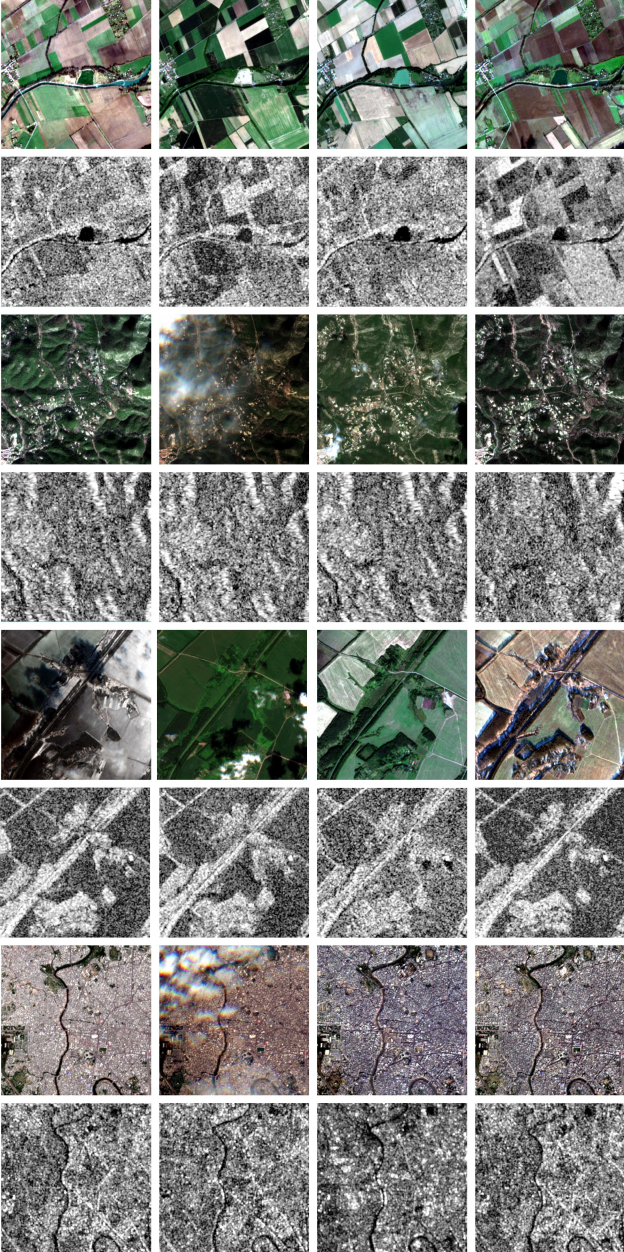


Figure 5: **Sample visualization of the SSL4EO-S12 dataset.** Odd-numbered rows represent Sentinel-2 (multi-spectral), and even-numbered rows represent Sentinel-1 (SAR). Each location is documented with four seasonal snapshots.

expand pretraining to include the entire dataset throughout 200 epochs. We utilize the computational resources of 8 NVIDIA GeForce RTX 4090 GPUs for the pretraining of our model. To ensure efficient computing, the images are resized to 128×128 pixels. Consistent with the normalization methods of the SSL4EO-S12 dataset [35], we adopt the same normalization standards. For data augmentation, we apply the partial overlap crop approach mentioned in Section 3.2, each with random horizontal flipping, as implemented in MAE [14]. The batch size is configured at 2048. The training employs the AdamW optimizer [43] with a base learning rate of 1×10^{-4} , which we modulate using a half-cycle cosine decay schedule [44] across 200 epochs.

4.2. Downstream optical experiments

We evaluate our model SeaMo across multiple optical datasets, focusing on tasks such as single/multi-label classification, change detection, and semantic segmentation. These datasets vary in terms of scale, image size, sample region, and sensor types. The results demonstrate that our model achieves competitive performance relative to various benchmarks. To ensure a fair comparison, we select a range of models for evaluation. The compared methods encompass traditional supervised approaches as well as foundation models that utilize different self-supervised methods and are pretrained on different remote sensing (RS) datasets.

4.2.1. Single-label classification

We selected the EuroSAT [45] and fMoW-Sentinel[13] datasets for scene classification, with the results displayed

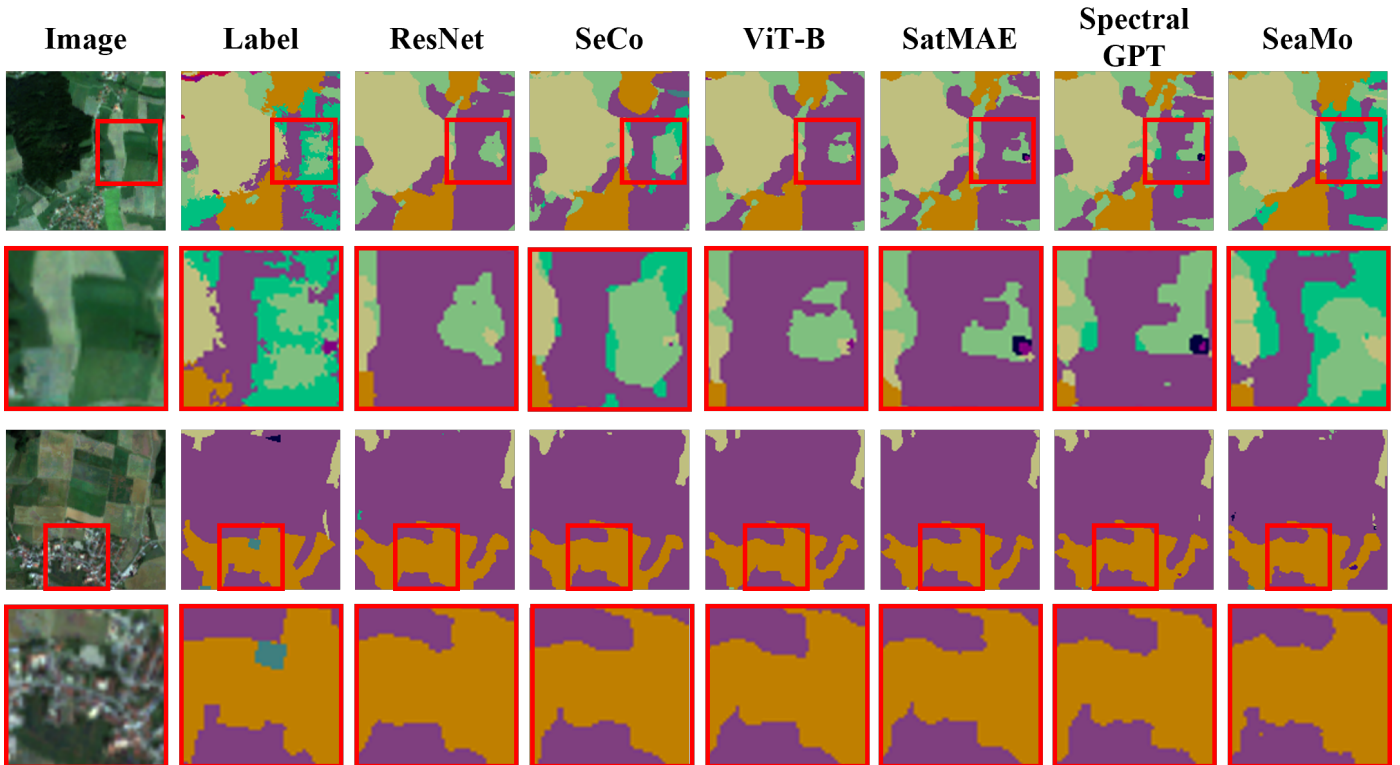


Figure 6: Visual results obtained by using different pre-trained foundation models for the downstream segmentation task on the SegMunich dataset.

in Table 1 and Table 2.

EuroSAT [45] is a dataset comprising 27,000 Sentinel-2 satellite images sourced from 34 European countries. These images are divided into 10 scene classification categories, with each category containing between 2,000 and 3,000 labeled images. Each image in the dataset has a resolution of 64×64 pixels and includes 13 spectral bands. In line with the methodologies used in SatMAE [13] and SpectralGPT [15], we exclude the cirrus band (B10) and utilize the remaining 12 bands for transfer learning. We utilized two NVIDIA GeForce RTX 4090 GPUs for our experiments on the EuroSAT dataset. Images were resized to 128×128 pixels. Data augmentation strategies mirrored those used in [13], including mixup [46] with a coefficient of 0.8, cutmix [47] of 1.0, and a drop path rate [48] of 0.2. The base learning rate was set at 10^{-2} , with a batch size of 512. Training was conducted over 150 epochs, which included 20 warm-up epochs, utilizing the AdamW optimizer [43]. The model employed soft cross entropy loss as

the loss function.

The fMoW-Sentinel dataset presents a more challenging scenario with its 63 categories and global sample strategy, resulting in larger performance discrepancies across models. We utilized only 10% of the training data for fine-tuning. The input images are resized to 128×128 pixels. The base learning rate is set to 2×10^{-4} . The training spanned 80 epochs, which included 20 warm-up epochs. The data augmentation techniques and loss function implementation were aligned with those used for the EuroSAT dataset. Remarkably, our model outperforms all others, including those fine-tuned with the full dataset. Notably, though SatMAE, which is pretrained and then fine-tuned on the fMoW-Sentinel, shows better results than other compared models, SeaMo still surpasses SatMAE [13], demonstrating superior generalization capabilities of our model.

4.2.2. Multi-label classification

We selected the BigEarthNet [49] dataset for multi-label land cover classification. The BigEarthNet (BigEarthNet-MM) dataset [50] consists of 590,326 pairs of Sentinel-1 and Sentinel-2 image patches, designed for multi-modal, multi-label remote sensing image classification. Each image pair is annotated with multi-labels from the CORINE Land Cover (CLC) map of 2018, utilizing the detailed Level-3 class nomenclature. The optical images in the dataset feature 12 multi-spectral channels. In line with practices from SpectralGPT [15], we excluded 12% of the images due to low quality. Consistent with previous studies [51], the dataset is divided into 354,196 training samples and 118,065 validation samples. The input images are resized to 128×128 pixels. We set the base learning rate to 10^{-5} and maintained a batch size of 512. The training spanned 50 epochs, which included 10 warm-up epochs, employing the AdamW optimizer [43] to optimize our model’s performance. All other implementation details remain consistent with those used in the fMoW-Sentinel optical task. In line with the approach used by SpectralGPT [15], we fine-tuned our model using only 10% of the training data. Our model achieved a mean Average Precision (mAP) of 88.54, outperforming all other models. Notably, despite SpectralGPT being pretrained specifically on the BigEarthNet dataset, our model still surpassed its performance, achieving the state-of-the-art (SOTA) among all comparable scale models.

4.2.3. Semantic segmentation

We selected the DFC2020 [52] and SegMunich [15] datasets to evaluate our model on optical Sentinel-2 segmentation tasks.

The 2020 IEEE GRSS Data Fusion Contest [52] offers a high-quality global land-cover multi-modal dataset comprising 8 classes. We utilize the dataset provided by Anthony Fuller et al. [18]. This dataset has been preprocessed to include 46,152 training images and 8,874 vali-

Table 3: **Fine-tuning (FT) Results on DFC2020 segmentation dataset.** CL represents the contrastive learning method and MAE represents the masked autoencoder method.

Model	Pretrain Method	Backbone	mIOU
GASSL	CL	ResNet50	34.25
SeCo	CL	ResNet50	36.49
DINO	CL	ViT-S	32.34
SatMAE	MAE	ViT-B	45.53
SpectralGPT	MAE	ViT-B	44.36
CROMA	MAE&CL	ViT-B	46.67
SatMAE	MAE	ViT-L	46.15
SeaMo	MAE	ViT-B	49.79

Table 4: **Fine-tuning (FT) results on SegMunich segmentation dataset.** CL represents the contrastive learning method and MAE represents the masked autoencoder method.

Model	Pretrain Method	Backbone	mIOU
GASSL	CL	ResNet50	45.6
SeCo	CL	ResNet50	45.9
DINO	CL	ViT-S	46.5
SatMAE	MAE	ViT-B	48.7
SpectralGPT	MAE	ViT-B	49.8
SatMAE	MAE	ViT-L	50.7
SpectralGPT	MAE	ViT-L	51.0
CROMA	MAE&CL	ViT-B	51.1
SeaMo	MAE	ViT-B	51.3

dation images, with each image resized to 96×96 pixels. We utilized two NVIDIA GeForce RTX 4090 GPUs for our experiments on the DFC2020 dataset. We maintain the original image size of the dataset at 96×96 pixels without resizing. Data augmentation is limited to random vertical and horizontal flips, each with a probability of 0.5. For the optical data task, the base learning rate is set at 1×10^{-4} . We fine-tune our model on the optical dataset for 30 epochs, including 5 warm-up epochs. The batch size is set to 64, and we use the soft cross entropy loss as the loss function. The results, displayed in Table 3, highlight SeaMo’s performance, achieving a mean Intersection over Union (mIoU) of 49.79, which is 3.12 points higher than the second-best performing model.

The SegMunich dataset [15] consists of a 10-band Sentinel-2 image composite, with dimensions of $3,847 \times 2,958$ pixels and a spatial resolution of 10 meters. It cap-

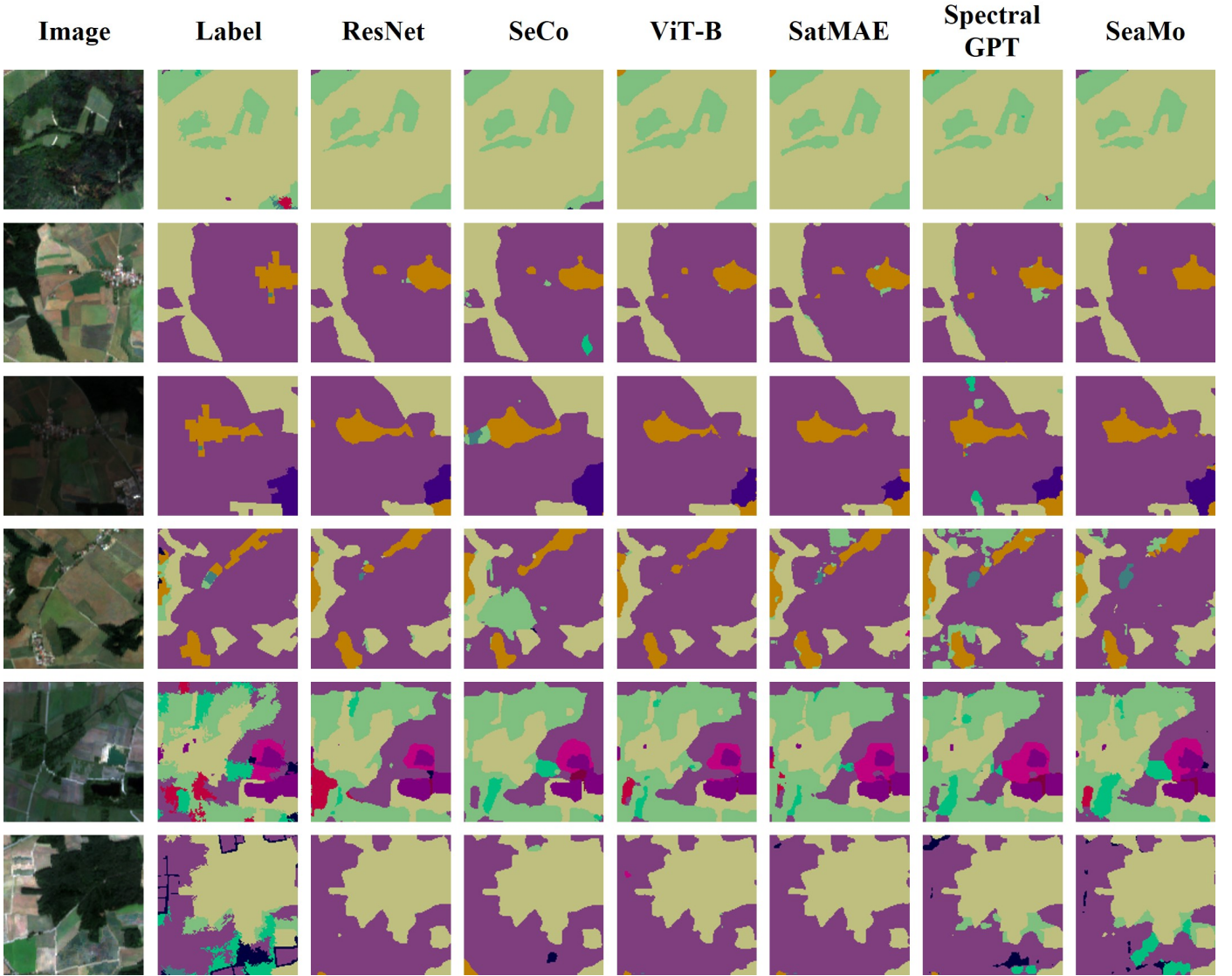


Figure 7: More visual results obtained by using different pre-trained foundation models for the downstream semantic segmentation task on the SegMunich dataset.

tures the urban landscape of Munich over three years and includes a segmentation mask that accurately delineates 13 Land Use and Land Cover (LULC) classes. We processed the image data into 128×128 pixel tokens with a 50% overlap, following the dataset split introduced in [15]. For downstream experiments on the SegMunich dataset, we utilized four NVIDIA GeForce RTX 4090 GPUs. The base learning rate was set at 1×10^{-4} and the batch size at 128. The model underwent training for 100 epochs to ensure convergence and optimal results. Data augmentation and the loss function were consistent with those used

in the DFC2020 tasks. Figure 6, 7 and 10 display representative visualizations illustrating the performance of our model and other comparative methods on the respective datasets. The results are displayed in Table 4. SeaMo not only performs exceptionally on this dataset but also achieves state-of-the-art (SOTA) results compared to other models. This demonstrates SeaMo’s robust capability in handling complex urban segmentation tasks.

4.2.4. Change Detection

Urban change detection is a crucial task in remote sensing (RS) applications. We chose to evaluate our model us-

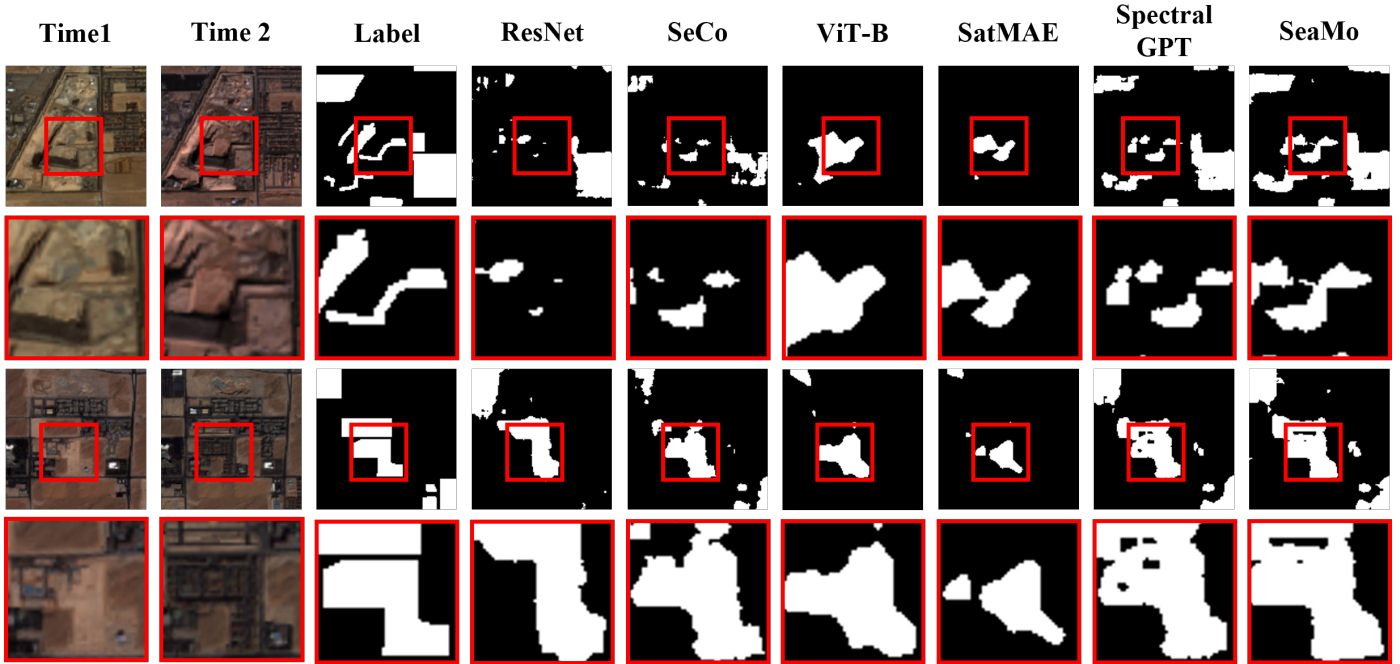


Figure 8: Visual results obtained by using different pre-trained foundation models for the downstream change detection task on the OSCD dataset.

Table 5: **Fine-tuning (FT) results on OSCD change detection dataset.** CL represents the contrastive learning method and MAE represents the masked autoencoder method.

Model	Pretrain Method	Backbone	F1 Score
SSL4EO	CL	ResNet18	41.85
GASSL	CL	ResNet50	46.26
SeCo	CL	ResNet50	47.67
CaCO	CL	ResNet50	52.11
DINO-MC	CL	ViT-S	52.70
ViT-22k	Supervised	ViT-B	52.23
SatMAE	MAE	ViT-B	52.76
SpectralGPT	MAE	ViT-B	54.29
SeaMo	MAE	ViT-B	54.54

ing the Onera Satellite Change Detection (OSCD) dataset [53]. The OSCD dataset comprises 24 pairs of Sentinel-2 images from the period 2015 to 2018. It includes 14 training and 10 evaluation images, each with 13 spectral bands across resolutions of 10m, 20m, and 60m. Labels within this dataset specify pixel-level urban changes. Following the approach used in SpectralGPT [15], we segmented the image data into 128×128 pixel tokens with a 50% overlap. For the experiments on the OSCD dataset, we utilized four NVIDIA GeForce RTX 4090 GPUs. Data augmenta-

tion was limited to random flipping and random rotation to maintain the integrity of the change detection features. The model was trained over 50 epochs, with a batch size of 128 and a learning rate set at 1×10^{-4} . We employed negative log-likelihood loss (NLLoss) as the training objective to optimize model performance effectively. According to results presented in Table 5, our model achieved the highest F1-score of 54.54 compared to other models. Figure 8 and 9 display representative visualizations illustrating the performance of our model and other comparative methods on the respective datasets.

While SeaMo shows promising results, it does not currently qualify as the state-of-the-art (SOTA) model on this dataset. The reason might be the inadequate employment of the segmentation head and the backbone, and potential issues arising from data imbalance. The complexity of the ViT architecture employed requires significant data to effectively counteract overfitting. Currently, we utilize the UperNet head, which differentiates between the output features of two urban images for change detection purposes. In future developments, we aim to extensively

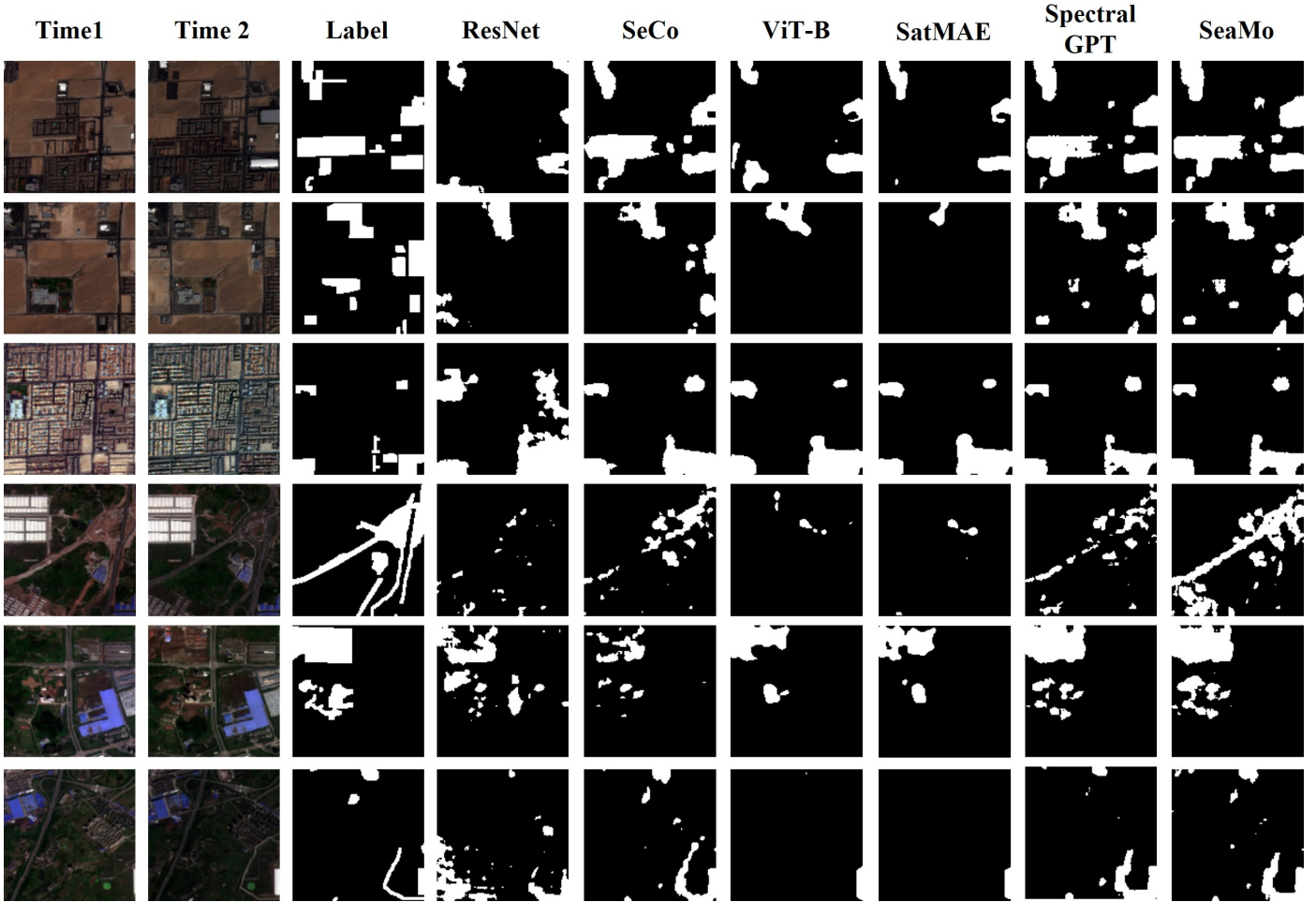


Figure 9: More visual results obtained by using different pre-trained foundation models for the downstream change detection task on the OSCD dataset.

explore and refine the segmentation head specifically tailored for change detection tasks. This will involve addressing both architectural and data-related challenges to enhance model performance and establish new benchmarks for SOTA results in this domain.

4.3. Downstream radar experiments

In addition to evaluating SeaMo on optical downstream tasks, we have extended our assessments to include radar-sourced tasks, comparing its performance against several advanced models. These evaluations encompass single/multi-label classification and semantic segmentation tasks. To ensure a fair comparison, we chose models for evaluation that were either pretrained on multi-modal or exclusively on radar data. The results confirm

that SeaMo also excels in radar-based tasks, demonstrating its versatility and robust performance across various data sources.

4.3.1. Single/Multi-label classification.

Table 6: **Fine-tuning (FT) results on EuroSAT-SAR dataset.** CL represents the contrastive learning method and MAE represents the masked autoencoder method.

Model	Pretrain Method	Backbone	Top1 Acc.
SSL4EO-MAE	MAE	ViT-S	81.05
DINO-MM	CL	ViT-S	85.43
FGMAE	MAE	ResNet50	85.90
CROMA	MAE	ViT-B	88.42
DOFA	MAE	ViT-B	88.59
SeaMo	MAE	ViT-B	89.69

For this set of tasks, we selected the EuroSAT-SAR [54]

and BigEarthNet-SAR [50] datasets.

Wang et al. [54] collected the SAR modality dataset, which corresponds to the optical multispectral EuroSAT [45] dataset. We employ the same hyper-parameter settings as those used in the EuroSAT-Optical dataset [45]. Table 6 presents the results of our model alongside those of the compared models.

BigEarthNet-SAR corresponds to the optical dataset and forms part of the BigEarthNet-MultiModal (MM) dataset. As with the optical tasks, we fine-tuned only 10% of the training data from BigEarthNet-SAR. For tasks on the BigEarthNet-SAR dataset, we set the base learning rate to 8×10^{-5} and kept all other settings consistent with those used in the optical task. Table 7 presents the results of our model alongside the compared models.

Due to the inherent differences in imaging mechanisms and quality, the performance of all models on SAR data is generally lower than on optical data. However, it is evident that our model significantly outperforms others in SAR tasks, achieving substantial improvements. Notably, the performance of SeaMo on BigEarthNet-SAR surpasses even the MAE model fine-tuned with the entire training dataset. These findings underscore that pretraining with multimodal data can enhance model performance on downstream unimodal tasks more effectively than pretraining with unimodal data, even when employing the same self-supervised method.

4.3.2. Semantic segmentation.

We selected the DFC 2020 dataset [52] for the SAR-modality segmentation task, which corresponds to the DFC 2020 optical dataset mentioned in Section 4.2. We maintain the original image size of the dataset at 96×96 pixels without resizing. Data augmentation is limited to random vertical and horizontal flips, each with a probability of 0.5. All the training settings are the same as those in the optical dataset. The results, presented in Table 8, show that SeaMo’s performance on this SAR-

Table 7: **Fine-tuning (FT) results on BigEarthNet-SAR dataset.** CL represents the contrastive learning method and MAE represents the masked autoencoder method. We default to using only 10% of the training data to fine-tune the models. * denotes the results obtained by fine-tuning with all training data, rather than only 10% of the data.

Model	Pretrain Method	Backbone	mAP
SSL4EO-MAE	MAE	ViT-S	74.90/81.30*
DINO-MM	CL	ViT-S	79.50*
FGMAE	MAE	ViT-S	78.05
SatViT	MAE	ViT-B	75.41*
FusMAE	MAE	ViT-B	75.50*
DOFA	MAE	ViT-B	81.46
CROMA	MAE	ViT-B	81.57
SeaMo	MAE	ViT-B	82.23

Table 8: **Fine-tuning (FT) results on DFC2020-SAR segmentation dataset.** CL represents the contrastive learning method and MAE represents the masked autoencoder method.

Model	Pretrain Method	Backbone	mIoU
SSL4EO-MAE	MAE	ViT-S	42.35
DINO-MM	CL	ViT-S	44.86
SatViT	MAE	ViT-B	46.27
CROMA	MAE	ViT-B	48.71
DOFA	MAE	ViT-B	49.18
SeaMo	MAE	ViT-B	49.54

modality dataset is comparable to its performance on the corresponding optical dataset, yet it still achieves SOTA with a mIoU of 49.54, which is 0.83 points higher than the second-best model. Additionally, consistent with our earlier observations, models pretrained with multimodal data consistently outperform those pretrained with SAR-only data.

Table 9: **Fine-tuning (FT) results on GLH-Water and S1S2-Water segmentation datasets.** S1S2-Water (S1) denotes fine-tuning performed on Sentinel-1 data, while S1S2-Water (S2) represents fine-tuning on Sentinel-2 data.

Model	GLH-Water		S1S2-Water (S1)		S1S2-Water (S2)	
	IoU	F1	IoU	F1	IoU	F1
UNet	82.7	90.2	87.5	90.2	94.2	96.9
ResNet	85.6	92.2	92.5	96.0	97.7	96.5
ViT	83.5	90.5	91.6	94.7	98.5	99.3
SeaMo	86.2	92.8	93.7	96.7	98.7	99.5

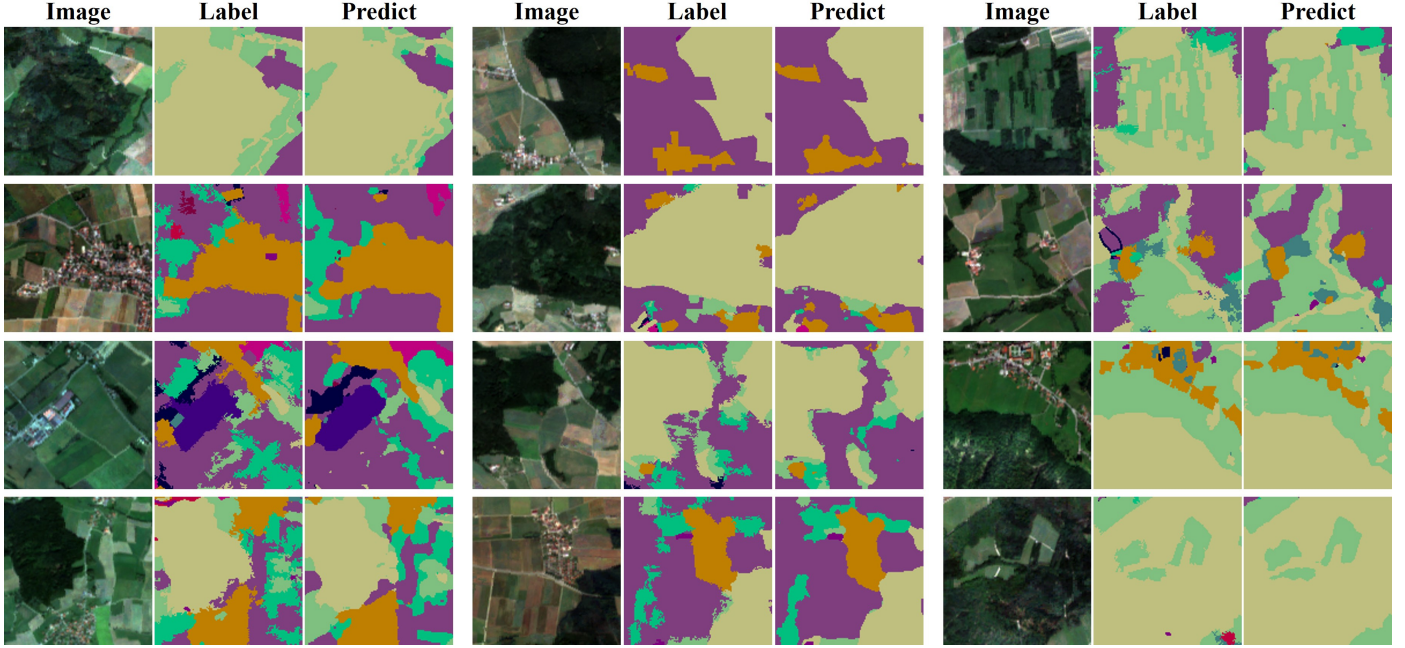


Figure 10: Additional visualizations of ground truth labels and SeaMo’s predicted results on the SegMunich dataset.

Table 10: Ablations studies of Crop strategies.

Ablation	Crop Rate	BEN-Optical	EuroSAT-Optical	BEN-SAR	EuroSAT-SAR	OCS D
		mAP	Top1 Acc.	Top1 Acc.	Top1 Acc.	F1 Score
Same Location	100%	87.19	99.07	81.57	87.70	49.56
Partial Overlap	[75%,100%]	88.40	99.30	81.96	89.41	53.94
Partial Overlap	[50%,100%]	88.54	99.37	82.23	89.69	54.54
Partial Overlap	[25%,100%]	88.44	99.35	82.10	89.55	54.13

Table 11: Ablations studies of Temporal-Multimodal blocks.

Ablation	BEN	EuroSAT	BEN-SAR	OCS D
	mAP	Top1 Acc.	Top1 Acc.	F1 Score
w/o TM Block	88.30	99.30	81.74	53.15
Decouple	88.46	99.41	82.30	53.94
Fuse (Default)	88.54	99.37	82.23	54.54

4.4. More downstream segmentation tasks

To further evaluate SeaMO’s feature extraction capabilities, we fine-tuned it on more specific remote sensing segmentation datasets focused on single-object recognition tasks. We selected the GLH-Water and S1-S2 Water datasets, dedicated to water body segmentation and encompassing different resolutions and modalities. Table 9 presents the performance of our model alongside the comparison methods on these datasets.

The GLH-Water dataset [55] consists of 250 high-resolution satellite images ($12,800 \times 12,800$ pixels at 0.3 meters) globally sourced and meticulously annotated for surface water features. These images capture a wide range of water bodies, including rivers, lakes, and ponds against diverse backdrops like forests, agricultural lands, barren terrains, and urban environments. Following the protocols in the original paper, we cropped these images without overlap, yielding 156,250 segmented images divided into 125,000 for training, 15,625 for validation, and 15,625 for testing. We fine-tuned SeaMO on this dataset over 30 epochs using four NVIDIA GeForce RTX 4090 GPUs, with data augmentation techniques and loss functions consistent with the DFC2020 task, a base learning rate of 1×10^{-4} , and a batch size of 24. Figure 11 illustrates

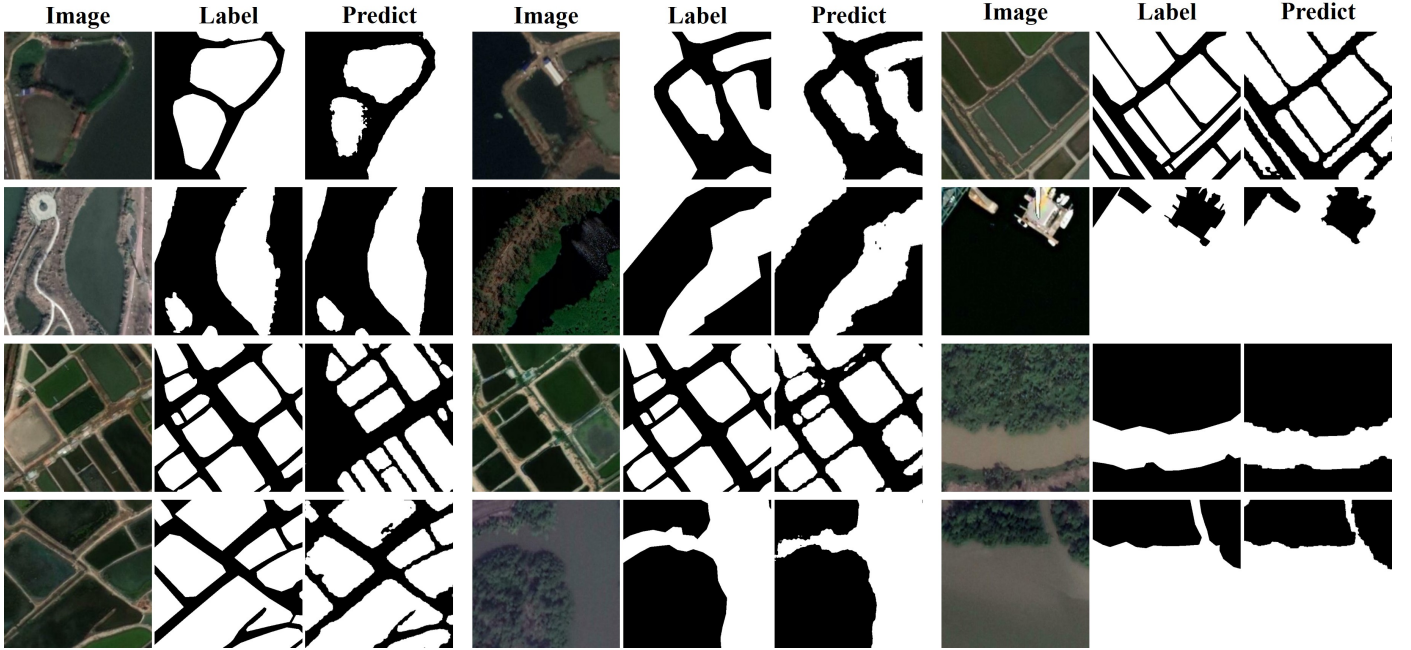


Figure 11: Visualizations of ground truth labels and SeaMo’s predicted results on the GLH-Water dataset.

SeaMO’s segmentation performance on the GLH-Water dataset.

S1-S2 Water [56] is a global reference dataset for semantic segmentation of surface water bodies using publicly available Sentinel-1 and Sentinel-2 images. It comprises 65 triplets of images with quality-checked binary water masks, resulting in over 50,000 non-overlapping 256×256 pixel patches for training and over 25,000 patches for validation and testing. Figures 12 and 13 show visualizations of test results after fine-tuning the training sets of Sentinel-1 and Sentinel-2 images. The training settings are the same as those in the GLH-Water implementation. Our model achieves excellent segmentation performance on both the high-resolution GLH-Water dataset and the S1-S2 Water dataset, demonstrating its robustness across different resolutions and modalities.

4.5. Ablation studies

We conducted ablation studies on SeaMo to delineate the contribution of each component under the default settings: the partial overlap crop within the crop rate from 75% to 100%, the fuse type temporal-multimodal block,

the Multimodal-Temporal-TM pretraining strategy, a decoder with four blocks, an independent mask ratio of 75%, reconstruction of normalized patches, and fixed sinusoidal positional embeddings. These studies spanned three tasks across different modalities. Notably, for fine-tuning purposes, we utilized only 10% of the training data from both the BigEarthNet optical and SAR datasets [50].

4.5.1. Ablation studies of Crop strategies

As described in Section 3.2, spatial cropping of images from different seasons can constrain the model to learn time-invariant spatial information more effectively. In Table 10, we employed various cropping strategies to investigate their impact on model performance. We maintained consistency in all variables except for spatial cropping, using multimodal inputs and incorporating a TM block architecture. In Table 10, **same location** means that images from all temporal phases are cropped from the same area, implying that, despite different random masking areas, the reconstruction always targets the same image. **Partial overlap** refers to randomly cropping a certain ratio of a larger image, ensuring that images from different

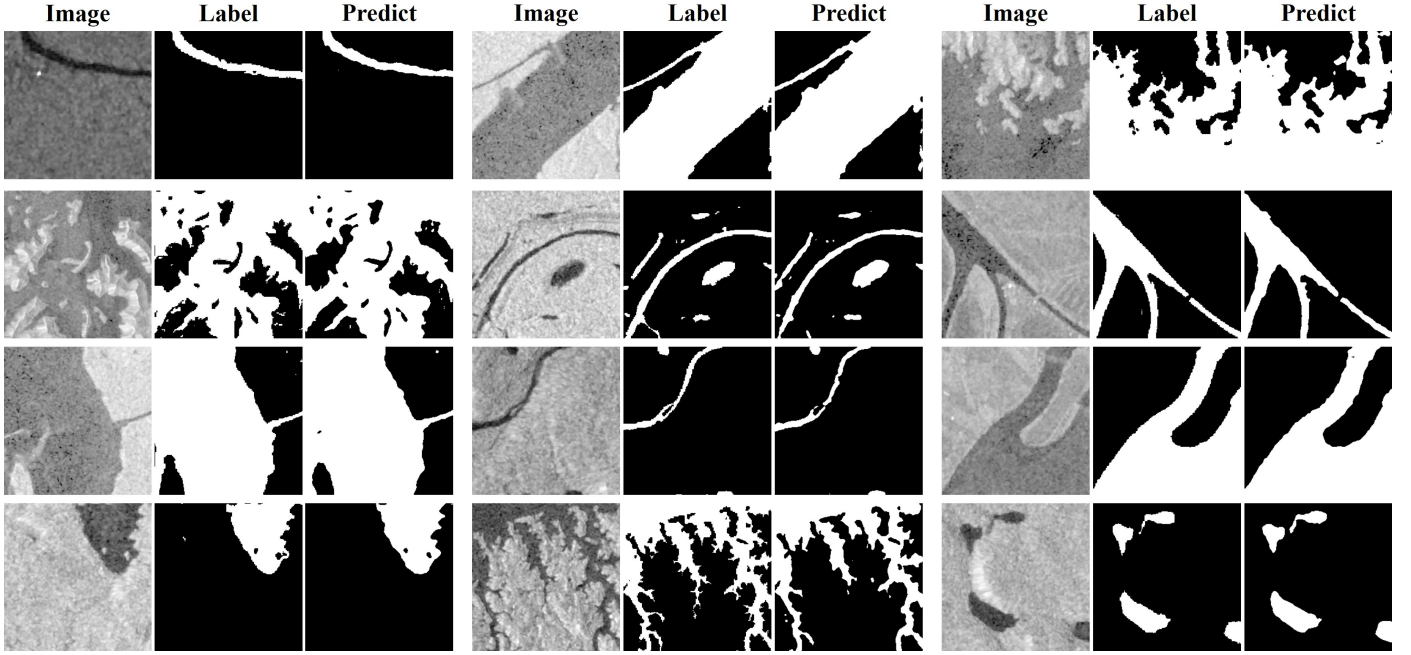


Figure 12: SAR visual comparisons of ground truth labels and SeaMo’s predicted results on the S1S2-Water dataset. We fine-tuned our model using only the Sentinel-1 data from the dataset.

temporal phases partially overlap. As the range of random cropping ratios increases, the overlap becomes more random, and it is even possible to have no overlap at all. The results demonstrate that the pretrained model performs best under our default condition with the TM Block when the overlap between data from different temporal phases is random but still maintains partial overlap. Performance declines when all temporal images are from the same region, which we attribute to the TM Block’s cross-attention mechanism allowing the model to easily optimize by reconstructing the same region from images at different times, thus inadequately mining spatial information. When the overlap area is excessively random, model performance slightly decreases. Overall, temporal data should maintain partial overlap rather than complete uniformity, as this increases the difficulty of the reconstruction task and better facilitates the learning of time-invariant spatial properties.

4.5.2. Ablation studies of Temporal-Multimodal blocks

We also conducted ablation studies on the design of Temporal-Multimodal (TM) blocks. Table 11 presents our

results. The model without TM blocks performs worse than the model with TM blocks, as also evidenced in Table 12. We explored two designs within the TM blocks: “decouple” and “fuse”.

As depicted in Figure 14, in the “fuse” design, a linear layer is used to fuse tokens from previous seasons with tokens from the current season. In this case, only one set of cross-attention layers is used. On the other hand, in the “decouple” design, tokens from previous seasons are not fused with tokens from the current season. Instead, two sets of independent cross-attention layers are used to interact with the modality tokens at the current season. Analyzing the results in Table 11, it is noteworthy that both the “decouple” and “fuse” designs perform better on some downstream tasks. However, considering that the “decouple” design requires more cross-attention layers, resulting in more model parameters and higher data dimensionality during TM blocks, as well as increased computational resources and longer training times, we choose the “fuse” design as the default setting.

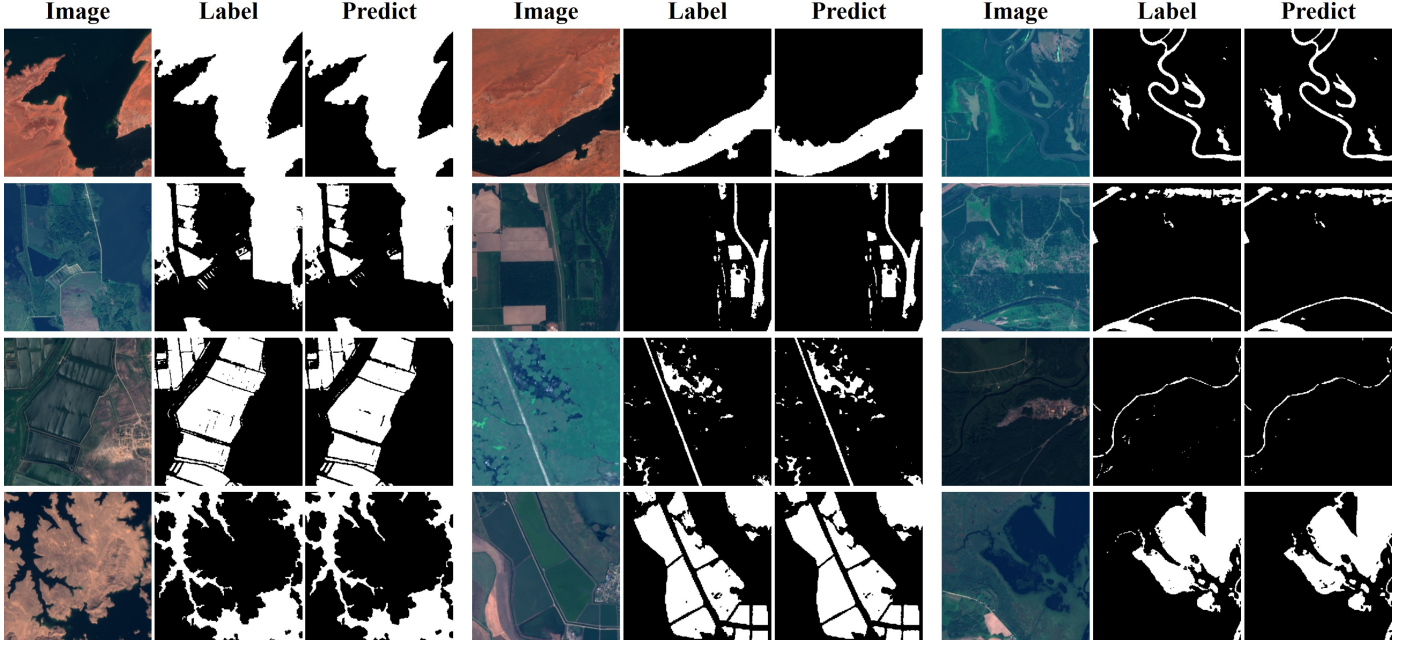


Figure 13: Optical visual comparisons of ground truth labels and SeaMo’s predicted results on the S1S2-Water dataset. We fine-tuned our model using only the Sentinel-2 data from the dataset.

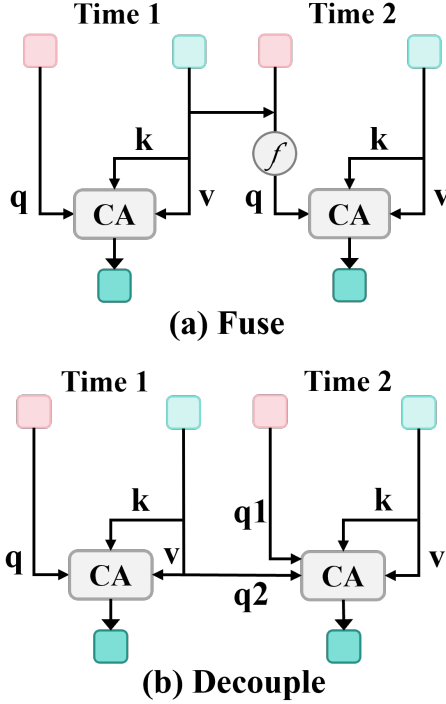


Figure 14: Different designs for Temporal-Multimodal blocks. (a) Fuse: In the “fuse” design, a linear layer is utilized to combine tokens from previous seasons with tokens from the current season. (b) Decouple: In the “decouple” design, two sets of independent cross-attention layers are employed to interact with the modality tokens of the current season.

Table 12: Ablation studies of pretraining strategy.

Ablation	BEN	EuroSAT	BEN-SAR
	mAP	Top1 Acc.	Top1 Acc.
Unimodal	-1.23	-0.09	-7.33
Multimodal	-0.73	-0.06	-0.99
Siamese	-1.01	-0.28	-2.40
Siamese-Temporal	-1.31	-0.22	+0.45
Unimodal-Temporal	-0.87	-0.11	-1.56
Multimodal-Temporal	-0.24	-0.07	-0.49
Multimodal-Temporal-TM	88.54	99.37	82.23

4.5.3. Pretraining strategy

Table 12 presents the performance of models pretrained with different strategies, with the Siamese and multimodal strategies illustrated in Figure 4. It is challenging to draw a definitive conclusion from these experiments, but we summarize the findings as follows: (1) All multimodal models consistently outperform their unimodal counterparts, suggesting that integrating multimodal data significantly enhances model performance. (2) Multimodal-based models generally surpass Siamese-based models across all optical tasks and most SAR tasks. We attribute this to the multimodal-based strategy’s effec-

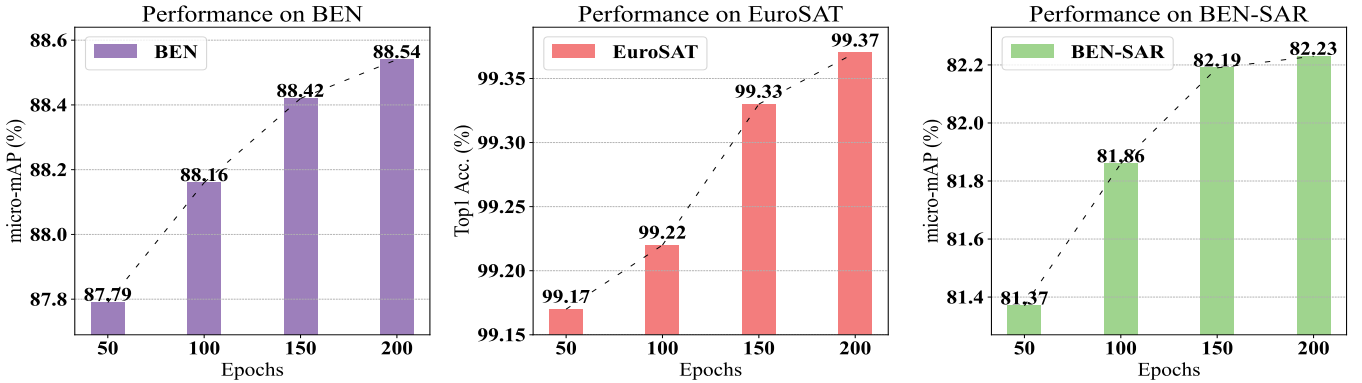


Figure 15: **Pretraining schedule.** We assessed SeaMo’s performance on BigEarthNet (optical & SAR) and EuroSAT datasets, finding that longer training significantly improves results.

Table 13: **Ablation Analysis of the proposed SeaMo in various aspects.** Highlighted entries represent the best results.

(a) Decoder Depth				(b) Mask Ratio			
Blocks	BEN	EuroSAT	BEN-SAR	Ratio	BEN	EuroSAT	BEN-SAR
	mAP	Top1 Acc.	mAP		mAP	Top1 Acc.	mAP
2	88.27	99.26	81.16	50%	88.26	99.24	81.45
4	88.54	99.37	82.23	75%	88.54	99.37	82.23
6	88.58	99.37	82.48	90%	88.38	99.22	81.09

(c) Reconstruction Target				(d) Positional Embedding			
Cases	BEN	EuroSAT	BEN-SAR	Type	BEN	EuroSAT	BEN-SAR
	mAP	Top1 Acc.	mAP		mAP	Top1 Acc.	mAP
w/o norm	87.45	99.31	81.25	learnable	88.34	99.35	82.11
w/ norm	88.54	99.37	82.23	sinusoidal	88.54	99.37	82.23

tive use of the self-attention mechanism in the encoder, which optimally fuses information across modalities. The only exception is the BEN-SAR task, where the Siamese-Temporal model performs best. We hypothesize that the Siamese architecture’s ability to preserve distinct properties of each modality is advantageous, particularly for datasets with lower imaging quality. (3) The inclusion of temporal information consistently benefits all models, corroborating our hypothesis that models equipped to capture time-invariant features can develop more generalized representations. (4) The TM block enhances the feature extraction capability, validating its necessity and effectiveness in our studies.

4.5.4. Model design ablations

Table 13 and Figure 15 present the results of our ablation studies, which range from model configuration adjustments to modifications in the pretraining schedule. The findings are summarized as follows:

(1) **Decoder depth:** A deeper decoder depth notably enhances model performance. However, considering the trade-off between complexity and benefit, we opted for a medium depth of 4 blocks as our default setting.

(2) **Mask ratio:** Table 13b shows the impact of varying the mask ratio. Unlike SpectralGPT, SeaMo exhibits decreased performance at a 90% mask ratio. This decline may be attributed to the already challenging nature of our pretraining pretext task and differences in tokenizer design.

(3) **Normalization:** Consistent with practices in MAE and SatMAE, reconstructing normalized patches has proven effective in enabling the encoder to learn more robust representations.

(4) **Positional embedding:** Both conventional learnable and fixed positional embeddings show minimal impact on model performance. In future iterations, we plan to explore more advanced embedding techniques to enhance model performance.

(5) **Pretraining length:** Figure 15 illustrates how pretraining length affects performance across three downstream tasks. It is evident that longer pretraining durations improve model performance, though the rate of improvement gradually diminishes. These ablation studies provide critical insights into the specific aspects of SeaMo that most significantly influence its effectiveness.

4.5.5. Generalizability test of the pretrained model

One distinguishing feature of RS images compared to natural images is the diversity in data types. For instance, spectral data captured by the same satellite can vary in image dimensions and the number of spectral bands depending on the preprocessing applied. Given that our model was pretrained on spectral images with dimensions of $128 \times 128 \times 12$, we aimed to assess its sensitivity to variations in image size and the number of spectral bands in downstream tasks. As described in Section 3, data entering the pretraining model must first pass through a modality-specific tokenizer to compress information. The weights of this tokenizer may not be suitable for different types of data. In our design, we opt for positional encoding interpolation for data of varying sizes, while for data with different channel counts, we introduce a new tokenizer. Although this approach does not utilize the original tokenizer’s pretrained weights, the features are still extracted through the pretrained backbone after projecting. Table 14 displays the performance of our pretrained model after fine-tuning on data with different image sizes and

Table 14: **Generalizability test of the model across different data types in the EuroSAT dataset.**

Case	Image Size	Spectral Band	Acc.
Case1	128×128	9	99.20
Case2	128×128	4	99.08
Case3	224×224	12	99.35
Case4	224×224	9	99.26
Default	128×128	12	99.37

spectral band counts. It is evident that while image size has minimal impact on model performance, a reduction in the number of bands significantly decreases performance. Therefore, future work will need to focus on designing a universal tokenizer that accommodates the diverse range of remote sensing data [42].

4.5.6. Compute

We estimate the computational resources required for both pretraining and fine-tuning our model, SeaMo, with the metrics presented in terms of RTX4090-24GB GPU hours. Detailed estimates are provided in Tab. 15.

Table 15: **Estimated GPU hours used for pretraining and finetuning SeaMo.**

Task	Dataset	GPU hours
Classification	EuroSAT (Optical&SAR)	6
Classification	fMoW Sentinel	20
Classification	BigEarthNet (Optical&SAR)	32
Change Detection	OSCD	2
Segmentation	SegMunich	32
Segmentation	DFC2020 (Optical&SAR)	20
Pretraining	SSL4EO-S12	200
Ablations	SSL4EO-S12	2050

5. Conclusion

In this paper, we introduce SeaMo, a foundation model for remote sensing (RS), pretrained in a self-supervised manner using a rich array of multi-seasonal and multi-modal data. SeaMo is equipped with feature-extracting encoders, temporal-multimodal fusion blocks (TM blocks), and image-reconstruction decoders. Under a progressive

masked image modeling framework, SeaMo utilizes space-unaligned heterogeneous satellite images to learn rich multimodal representations and leverage unimodal multi-seasonal satellite images to learn robust time-invariant spatial representations. SeaMo has demonstrated outstanding performance across a variety of downstream tasks, successfully handling several tasks across optical and SAR datasets, showing great potential for broader RS applications. Key insights from our work include: (1) The design of the foundation model architecture is crucial for learning the relationships between multiple RS properties, such as temporal-multimodal and spatial-temporal properties. (2) A progressive self-supervised pretraining approach, which gradually increases data complexity and refines training strategies, enables the model to develop robust representations at various stages. Looking ahead, we plan to expand our dataset by collecting more multimodal and multi-source data and to scale up the model to ViT-Large and ViT-Huge configurations. Additionally, we aim to enhance SeaMo’s performance by exploring more advanced tokenizer strategies and positional embeddings. We hope this work offers valuable insights into the development of foundation models for RS imagery.

Acknowledgements

This work was supported by the National Natural Science Foundation of China under Grant 42271350 and also supported by the International Partnership Program of the Chinese Academy of Sciences under Grant No.313GJHZ2023066FN. The numerical calculations in this study were carried out on the ORISE Supercomputer.

References

- [1] D. Hong, C. Li, B. Zhang, N. Yokoya, J. A. Benediktsson, J. Chanussot, Multimodal artificial intelligence foundation models: Unleashing the power of remote sensing big data in earth observation, *The Innovation Geoscience* 2 (1) (2024) 100055.
- [2] E. Rolf, K. Klemmer, C. Robinson, H. Kerner, Mission critical—satellite data is a distinct modality in machine learning, *arXiv preprint arXiv:2402.01444*.
- [3] C. Li, D. Hong, B. Zhang, T. Liao, N. Yokoya, P. Ghamisi, M. Chen, L. Wang, J. A. Benediktsson, J. Chanussot, Interpretable foundation models as decryptor peering into earth system, *The Innovation* (2024) 100682.
- [4] X. Wu, D. Hong, J. Chanussot, Convolutional neural networks for multimodal remote sensing data classification, *IEEE Transactions on Geoscience and Remote Sensing* 60 (2021) 1–10.
- [5] Y. Xu, T. Bai, W. Yu, S. Chang, P. M. Atkinson, P. Ghamisi, Ai security for geoscience and remote sensing: Challenges and future trends, *IEEE Geoscience and Remote Sensing Magazine* 11 (2) (2023) 60–85.
- [6] R. Bommasani, D. A. Hudson, E. Adeli, R. Altman, S. Arora, S. von Arx, M. S. Bernstein, J. Bohg, A. Bosselut, E. Brunskill, et al., On the opportunities and risks of foundation models, *arXiv preprint arXiv:2108.07258*.
- [7] X. Wanyan, S. Seneviratne, S. Shen, M. Kirley, Extending global-local view alignment for self-supervised learning with remote sensing imagery, in: *Proc. CVPR, 2024*, pp. 2443–2453.
- [8] D. Wang, Q. Zhang, Y. Xu, J. Zhang, B. Du, D. Tao, L. Zhang, Advancing plain vision transformer towards remote sensing foundation model, *IEEE Transactions on Geoscience and Remote Sensing*.
- [9] X. Li, D. Hong, J. Chanussot, S2mae: A spatial-spectral pre-training foundation model for spectral remote sensing data, in: *Proc. CVPR, 2024*, pp. 24088–24097.
- [10] O. Manas, A. Lacoste, X. Giró-i Nieto, D. Vazquez, P. Rodriguez, Seasonal contrast: Unsupervised pre-training from uncurated remote sensing data, in: *Proc. ICCV, 2021*, pp. 9414–9423.
- [11] U. Mall, B. Hariharan, K. Bala, Change-aware sampling and contrastive learning for satellite images, in: *Proc. CVPR, 2023*, pp. 5261–5270.
- [12] X. Sun, P. Wang, W. Lu, Z. Zhu, X. Lu, Q. He, J. Li, X. Rong, Z. Yang, H. Chang, et al., Ringmo: A remote sensing foundation model with masked image modeling, *IEEE Transactions on Geoscience and Remote Sensing*.
- [13] Y. Cong, S. Khanna, C. Meng, P. Liu, E. Rozi, Y. He, M. Burke, D. Lobell, S. Ermon, Satmae: Pre-training transformers for temporal and multi-spectral satellite imagery, *Proc. NeurIPS* 35 (2022) 197–211.
- [14] K. He, X. Chen, S. Xie, Y. Li, P. Dollár, R. Girshick, Masked autoencoders are scalable vision learners, in: *Proc. CVPR, 2022*, pp. 16000–16009.
- [15] D. Hong, B. Zhang, X. Li, Y. Li, C. Li, J. Yao, N. Yokoya, H. Li, P. Ghamisi, X. Jia, et al., Spectralgpt: Spectral remote sensing

- foundation model, *IEEE Transactions on Pattern Analysis and Machine Intelligence* 46 (8) (2024) 5227–5244.
- [16] C. J. Reed, R. Gupta, S. Li, S. Brockman, C. Funk, B. Clipp, K. Keutzer, S. Candido, M. Uyttendaele, T. Darrell, Scale-mae: A scale-aware masked autoencoder for multiscale geospatial representation learning, in: *Proc. ICCV*, 2023, pp. 4088–4099.
- [17] M. Noman, M. Naseer, H. Cholakkal, R. M. Anwar, S. Khan, F. S. Khan, Rethinking transformers pre-training for multi-spectral satellite imagery, arXiv preprint arXiv:2403.05419.
- [18] A. Fuller, K. Millard, J. Green, Croma: Remote sensing representations with contrastive radar-optical masked autoencoders, *Proc. NeurIPS* 36.
- [19] X. Guo, J. Lao, B. Dang, Y. Zhang, L. Yu, L. Ru, L. Zhong, Z. Huang, K. Wu, D. Hu, et al., Skysense: A multi-modal remote sensing foundation model towards universal interpretation for earth observation imagery, arXiv preprint arXiv:2312.10115.
- [20] B. Han, S. Zhang, X. Shi, M. Reichstein, Bridging remote sensors with multisensor geospatial foundation models, arXiv preprint arXiv:2404.01260.
- [21] C. Doersch, A. Gupta, A. A. Efros, Unsupervised visual representation learning by context prediction, in: *Proc. ICCV*, 2015, pp. 1422–1430.
- [22] N. Srivastava, E. Mansimov, R. Salakhudinov, Unsupervised learning of video representations using lstms, in: *Proc. ICML*, PMLR, 2015, pp. 843–852.
- [23] C. Vondrick, H. Pirsiavash, A. Torralba, Anticipating visual representations from unlabeled video, in: *Proc. CVPR*, 2016, pp. 98–106.
- [24] C. Vondrick, A. Shrivastava, A. Fathi, S. Guadarrama, K. Murphy, Tracking emerges by coloring videos, in: *Proc. ECCV*, 2018, pp. 391–408.
- [25] T. Chen, S. Kornblith, M. Norouzi, G. Hinton, A simple framework for contrastive learning of visual representations, in: *Proc. ICML*, PMLR, 2020, pp. 1597–1607.
- [26] K. He, H. Fan, Y. Wu, S. Xie, R. Girshick, Momentum contrast for unsupervised visual representation learning, in: *Proc. CVPR*, 2020, pp. 9729–9738.
- [27] Z. Xie, Z. Zhang, Y. Cao, Y. Lin, J. Bao, Z. Yao, Q. Dai, H. Hu, Simmim: A simple framework for masked image modeling, in: *Proc. CVPR*, 2022, pp. 9653–9663.
- [28] C. Tao, X. Zhu, W. Su, G. Huang, B. Li, J. Zhou, Y. Qiao, X. Wang, J. Dai, Siamese image modeling for self-supervised vision representation learning, in: *Proc. CVPR*, 2023, pp. 2132–2141.
- [29] Q. Zhou, C. Yu, H. Luo, Z. Wang, H. Li, Mimco: Masked image modeling pre-training with contrastive teacher, in: *Proc. ACM MM*, 2022, pp. 4487–4495.
- [30] S. Alaparthy, M. Mishra, Bidirectional encoder representations from transformers (bert): A sentiment analysis odyssey, arXiv preprint arXiv:2007.01127.
- [31] R. Bachmann, D. Mizrahi, A. Atanov, A. Zamir, Multimae: Multi-modal multi-task masked autoencoders, in: *Proc. ECCV*, Springer, 2022, pp. 348–367.
- [32] C. Feichtenhofer, Y. Li, K. He, et al., Masked autoencoders as spatiotemporal learners, *Proc. NeurIPS* 35 (2022) 35946–35958.
- [33] L. Zhou, H. Liu, J. Bae, J. He, D. Samaras, P. Prasanna, Self pre-training with masked autoencoders for medical image classification and segmentation, in: *Proc. ISBI*, IEEE, 2023, pp. 1–6.
- [34] T. Nguyen, J. Brandstetter, A. Kapoor, J. K. Gupta, A. Grover, Climax: A foundation model for weather and climate, arXiv preprint arXiv:2301.10343.
- [35] Y. Wang, N. A. A. Braham, Z. Xiong, C. Liu, C. M. Albrecht, X. X. Zhu, Ssl4eo-s12: A large-scale multimodal, multitemporal dataset for self-supervised learning in earth observation [software and data sets], *IEEE Geoscience and Remote Sensing Magazine* 11 (3) (2023) 98–106.
- [36] A. Vaswani, N. Shazeer, N. Parmar, J. Uszkoreit, L. Jones, A. N. Gomez, L. Kaiser, I. Polosukhin, Attention is all you need, *Proc. NeurIPS* 30.
- [37] A. Dosovitskiy, L. Beyer, A. Kolesnikov, D. Weissenborn, X. Zhai, T. Unterthiner, M. Dehghani, M. Minderer, G. Heigold, S. Gelly, J. Uszkoreit, N. Houlsby, An image is worth 16x16 words: Transformers for image recognition at scale, *Proc. ICLR*.
- [38] A. Gupta, J. Wu, J. Deng, L. Fei-Fei, Siamese masked autoencoders, arXiv preprint arXiv:2305.14344.
- [39] A. Eymaël, R. Vandeghen, A. Cioppa, S. Giancola, B. Ghanem, M. Van Droogenbroeck, Efficient image pre-training with siamese cropped masked autoencoders, arXiv preprint arXiv:2403.17823.
- [40] M. Mendieta, B. Han, X. Shi, Y. Zhu, C. Chen, Towards geospatial foundation models via continual pretraining, in: *Proc. ICCV*, 2023, pp. 16806–16816.
- [41] L. Wang, B. Huang, Z. Zhao, Z. Tong, Y. He, Y. Wang, Y. Wang, Y. Qiao, Videomae v2: Scaling video masked autoencoders with dual masking, in: *Proc. CVPR*, 2023, pp. 14549–14560.
- [42] Z. Xiong, Y. Wang, F. Zhang, A. J. Stewart, J. Hanna, D. Borth, I. Papoutsis, B. L. Saux, G. Camps-Valls, X. X. Zhu, Neural plasticity-inspired foundation model for observing the earth crossing modalities, arXiv preprint arXiv:2403.15356.
- [43] I. Loshchilov, F. Hutter, Decoupled weight decay regularization, in: *Proc. ICLR*, 2018.
- [44] I. Loshchilov, F. Hutter, Sgdr: Stochastic gradient descent with warm restarts, in: *Proc. ICLR*, 2016.
- [45] P. Helber, B. Bischke, A. Dengel, D. Borth, Eurosat: A novel

- dataset and deep learning benchmark for land use and land cover classification, *IEEE Journal of Selected Topics in Applied Earth Observations and Remote Sensing* 12 (7) (2019) 2217–2226.
- [46] H. Zhang, M. Cisse, Y. N. Dauphin, D. Lopez-Paz, mixup: Beyond empirical risk minimization, in: *Proc. ICLR*, 2018.
- [47] S. Yun, D. Han, S. J. Oh, S. Chun, J. Choe, Y. Yoo, Cutmix: Regularization strategy to train strong classifiers with localizable features, in: *Proc. ICCV*, 2019, pp. 6023–6032.
- [48] G. Huang, Y. Sun, Z. Liu, D. Sedra, K. Q. Weinberger, Deep networks with stochastic depth, in: *Proc. ECCV*, Springer, 2016, pp. 646–661.
- [49] G. Sumbul, M. Charfuelan, B. Demir, V. Markl, Bigearthnet: A large-scale benchmark archive for remote sensing image understanding, in: *Proc. IGARSS, IEEE*, 2019, pp. 5901–5904.
- [50] G. Sumbul, A. De Wall, T. Kreuziger, F. Marcelino, H. Costa, P. Benevides, M. Caetano, B. Demir, V. Markl, Bigearthnet-mm: A large-scale, multimodal, multilabel benchmark archive for remote sensing image classification and retrieval [software and data sets], *IEEE Geoscience and Remote Sensing Magazine* 9 (3) (2021) 174–180.
- [51] M. Neumann, A. S. Pinto, X. Zhai, N. Houlsby, In-domain representation learning for remote sensing, *arXiv preprint arXiv:1911.06721*.
- [52] C. Robinson, K. Malkin, N. Jovic, H. Chen, R. Qin, C. Xiao, M. Schmitt, P. Ghamisi, R. Hänsch, N. Yokoya, Global land-cover mapping with weak supervision: Outcome of the 2020 IEEE GRSS Data Fusion Contest, *IEEE Journal of Selected Topics in Applied Earth Observations and Remote Sensing* 14 (2021) 3185–3199.
- [53] R. C. Daudt, B. Le Saux, A. Boulch, Y. Gousseau, Urban change detection for multispectral earth observation using convolutional neural networks, in: *Proc. IGARSS, IEEE*, 2018, pp. 2115–2118.
- [54] Y. Wang, H. H. Hernández, C. M. Albrecht, X. X. Zhu, Feature guided masked autoencoder for self-supervised learning in remote sensing, *arXiv preprint arXiv:2310.18653*.
- [55] Y. Li, B. Dang, W. Li, Y. Zhang, Glh-water: A large-scale dataset for global surface water detection in large-size very-high-resolution satellite imagery, in: *Proc. AAAI*, Vol. 38, 2024, pp. 22213–22221.
- [56] M. Wieland, F. Fichtner, S. Martinis, S. Groth, C. Krullikowski, S. Plank, M. Motagh, S1s2-water: A global dataset for semantic segmentation of water bodies from sentinel-1 and sentinel-2 satellite images, *IEEE Journal of Selected Topics in Applied Earth Observations and Remote Sensing*.